Journal of Applied Geophysics 138 (2017) 114–126

Contents lists available at ScienceDirect

Journal of Applied Geophysics

journal homepage: www.elsevier.com/locate/jappgeo

Integrated geophysical investigations of Main Barton Springs, Austin, Texas, USA

By Mustafa Saribudak [a,*], Nico M. Hauwert [b]

[a] Environmental Geophysics Associates, Austin, TX, United States
[b] City of Austin Watershed Protection Department, Austin, TX, United States

ARTICLE INFO

Article history:
Received 16 July 2015
Received in revised form 15 December 2016
Accepted 4 January 2017
Available online 8 January 2017

Keywords:
Barton Springs
Karst
Edwards Aquifer
Fault
Groundwater flow
Geophysics

ABSTRACT

Barton Springs is a major discharge site for the Barton Springs Segment of the Edwards Aquifer and is located in Zilker Park, Austin, Texas. Barton Springs actually consists of at least four springs. The Main Barton Springs discharges into the Barton Springs pool from the Barton Springs fault and several outlets along a fault, from a cave, several fissures, and gravel-filled solution cavities on the floor of the pool west of the fault.

Surface geophysical surveys [resistivity imaging, induced polarization (IP), self-potential (SP), seismic refraction, and ground penetrating radar (GPR)] were performed across the Barton Springs fault and at the vicinity of the Main Barton Springs in south Zilker Park. The purpose of the surveys was two-fold: 1) locate the precise location of submerged conduits (caves, voids) carrying flow to Main Barton Springs; and 2) characterize the geophysical signatures of the fault crossing Barton Springs pool.

Geophysical results indicate significant anomalies to the south of the Barton Springs pool. A majority of these anomalies indicate a fault-like pattern, in front of the south entrance to the swimming pool. In addition, resistivity and SP results, in particular, suggest the presence of a large conduit in the southern part of Barton Springs pool. The groundwater flow-path to the Main Barton Springs could follow the locations of those resistivity and SP anomalies along the newly discovered fault, instead of along the Barton Springs fault, as previously thought.

1. Introduction

Barton Springs is the primary discharge of the Barton Springs Segment, discharging an average of 62 ft^3/s (1.74 m^3/s) over 36 years of continuous discharge measurement from 1978 to 2014 (Johns, 2015). Barton Springs actually consists of at least four spring clusters: Main Barton (Parthenia), Eliza, Old Mills (Zenobia) and Upper Barton springs. The federally-designated sole source aquifer provides the water supply to an estimated 60,000 people. Barton Springs is also the habitat for federally listed endangered aquatic salamanders, *Eurycea sosorum* and the blind *Eurycea waterlooensis*. The preservation of Barton Springs is sufficiently important for Austin citizens that the Save-Our-Springs water quality ordinance was petitioned and voted for in 1991, and $145 million in voter-approved bonds and grants were approved to purchase 22% of the recharge zone and 7% of the contributing zone for the Barton Springs Segment of the Edwards Aquifer (Thuesen, 2013).

The Edwards Aquifer is a highly permeable karstic limestone aquifer in Central Texas that is between 300 and 700 ft thick (90 and 200 m). It includes the Edwards Group and other associated limestone and consists of three segments: 1) The San Antonio segment of the Aquifer extends in a 160 mi (225 km) arch-shaped curve from the west to near Kyle in the northeast, and is between five and 40 mi (64 km) wide at the surface; 2) The Barton Springs segment extends from Kyle to south Austin; 3) the northern segment lies to the north of Austin (Fig. 1, taken from Musgrove and Banner, 2004).

Barton Springs Segment of the aquifer covers about 155 mi^2 (235 km^2) and is composed of limestone that is highly faulted, fractured, and dissolved, forming a very prolific karst aquifer ranging from 0 to 450 ft thick (0 to 137 m) (Rose, 1972). The groundwater basin that provides discharge to Barton Springs also use four hydrologic zones: Contributing, Recharge, Confined, and a Saline Zone (Fig. 2C, modified from Mahler and Lynch, 1999).

Dye-traced flow path studies show that the recharge water from Onion Creek, which is about 17 mi (56 km) to the southwest of Austin, can reach Barton Springs within 2 days (Fig. 2C; Hunt et al., 2005). This observation indicates that the ground water flows quickly through the well-connected conduits within the Edwards Aquifer (Hauwert, 2009). Groundwater tracing delineated three geochemically-distinct preferential flow paths of groundwater to Barton Springs: the Sunset Valley, Manchaca, and Saline–Water flow paths (Hauwert et al., 2004).

A reconnaissance geophysical study (2D resistivity, self-potential and conductivity) covering three of the Barton Springs (Main Barton,

* Corresponding author.
E-mail addresses: ega@pdq.net (B.M. Saribudak), Nico.Hauwert@austintexas.gov (N.M. Hauwert).

http://dx.doi.org/10.1016/j.jappgeo.2017.01.004
0926-9851/

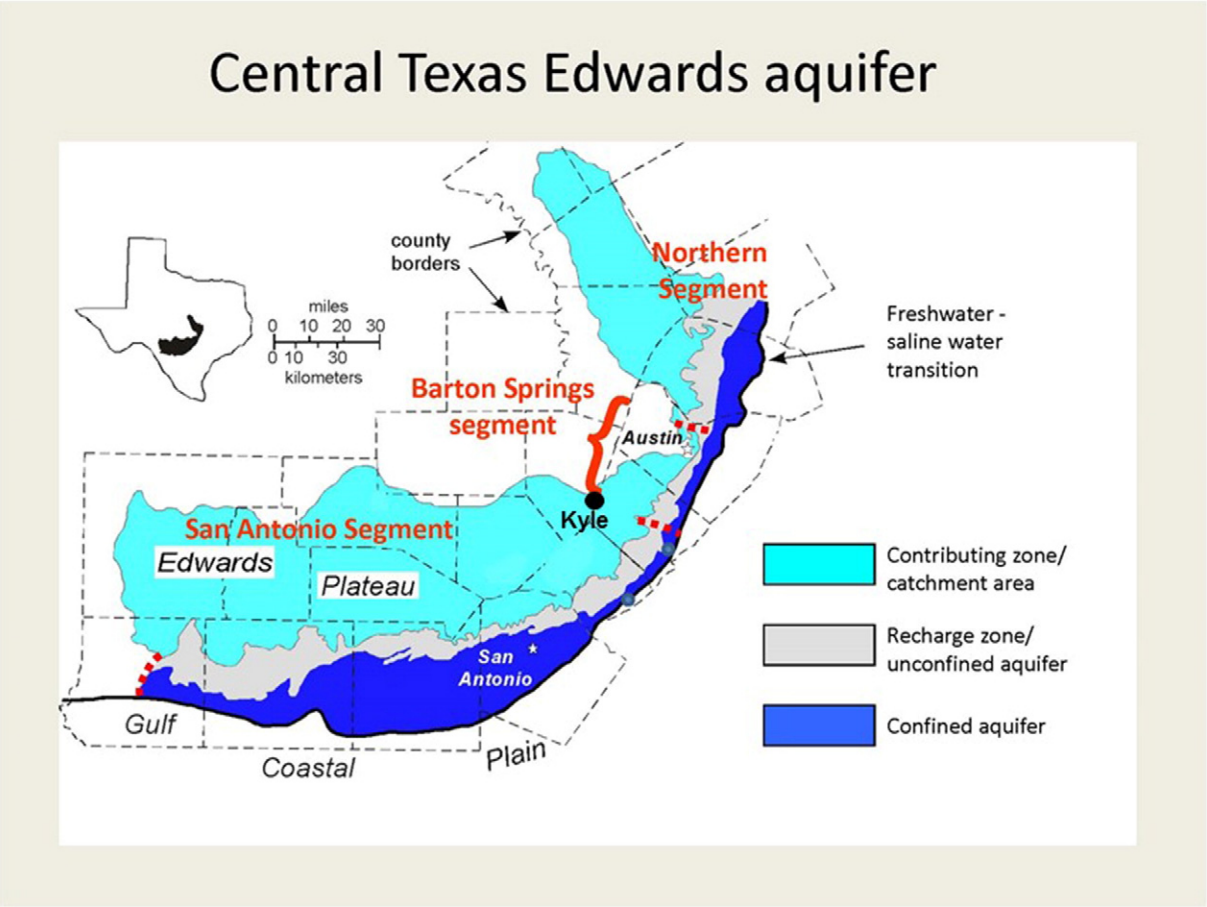

Fig. 1. Map showing the division of the San Antonio, Barton Springs and Northern segments of the Edwards Aquifer in Central Texas (Musgrove and Banner, 2004).

Eliza, and Old Mills) was conducted a few years ago (Saribudak et al., 2013). Results of this study indicated significant karst anomalies in the vicinity of the three springs. Especially in the Main Barton springs, resistivity and self-potential data hinted at a potential antithetic fault/conduit system in the south part of the Barton Springs Swimming pool, but there was not enough geophysical data to confirm it. Some of the resistivity and SP profiles from this work was included in this study.

In this current study, however, integrated geophysical surveys [2D and 3D resistivity, self-potential (SP), induced polarization (IP), seismic refraction tomography, and ground penetrating radar (GPR)] were performed in the vicinity of the Main Barton Springs and across the Barton Springs fault. The purpose of this additional field work was to: 1) determine the geophysical signature of the Barton Springs fault; and 2) define the suspected potential antithetic fault and conduit system, which could be the source for the ground water flow path for the Main Barton Springs.

2. Geology

Geological mapping of Austin by Garner et al. (1976) shows that faulting dominated the geology and physiography of the city and its environs. The Balcones escarpment, with a topographic relief as great as 300 ft (91 m) in Austin, is a fault-line scarp, marked by normal faults, which generally dip towards the east and southeast. The net fault offset is about 1100 ft (350 m; Hauwert, 2009, p.36). Thus, the structural framework of the Edwards Aquifer is controlled by the Balcones Fault Zone (BFZ), an echelon array of normal faults that has extended and dropped the aquifer and associated strata from northwest to the southeast across the three Segments (Small et al., 1996; Ferrill et al., 2005).

The surface geology of the Main Barton Springs area includes Edwards Aquifer units (regional dense and leached collapsed members) and the Georgetown Formation (Hauwert, 2009). Barton Springs fault juxtaposes the Edwards Group units against the Georgetown Formation (see Fig. 2A and B).

The estimated thickness of the regional dense member is 15 ft (4.5 m), the leached collapsed member is 15 ft (4.5 m), and the uneroded Georgetown formation is 45 ft (14 m). Based on these estimates, the offset of the Barton Springs Fault, separating the regional dense member and the Georgetown formation, is estimated to be, geologically, at least 20 ft (6 m) but less than 70 ft (21 m).

3. Geophysical methods

Integrated geophysical methods can provide new insights into the near-surface karstic features that Main Barton Springs and Barton Springs fault may contain. There have been a few geophysical studies published, which indicate the utilization of these methods across the Edwards Aquifer (Connor and Sandberg, 2001, Saribudak, 2011, Saribudak et al., 2012a, 2012b, 2013) and at other locations (e.g. Palmer, 2007, Carpenter, 1998, Ahmed and Carpenter, 2003, Dobecki and Upchurch, 2006).

3.1. Resistivity and induced polarization surveys

The 2D resistivity method images the subsurface by applying a constant current in the ground through two current electrodes and measuring the resulting voltage differences at two potential electrodes some distance away. An apparent resistivity value is the product of the measured resistance and a geometric correction for a given electrode

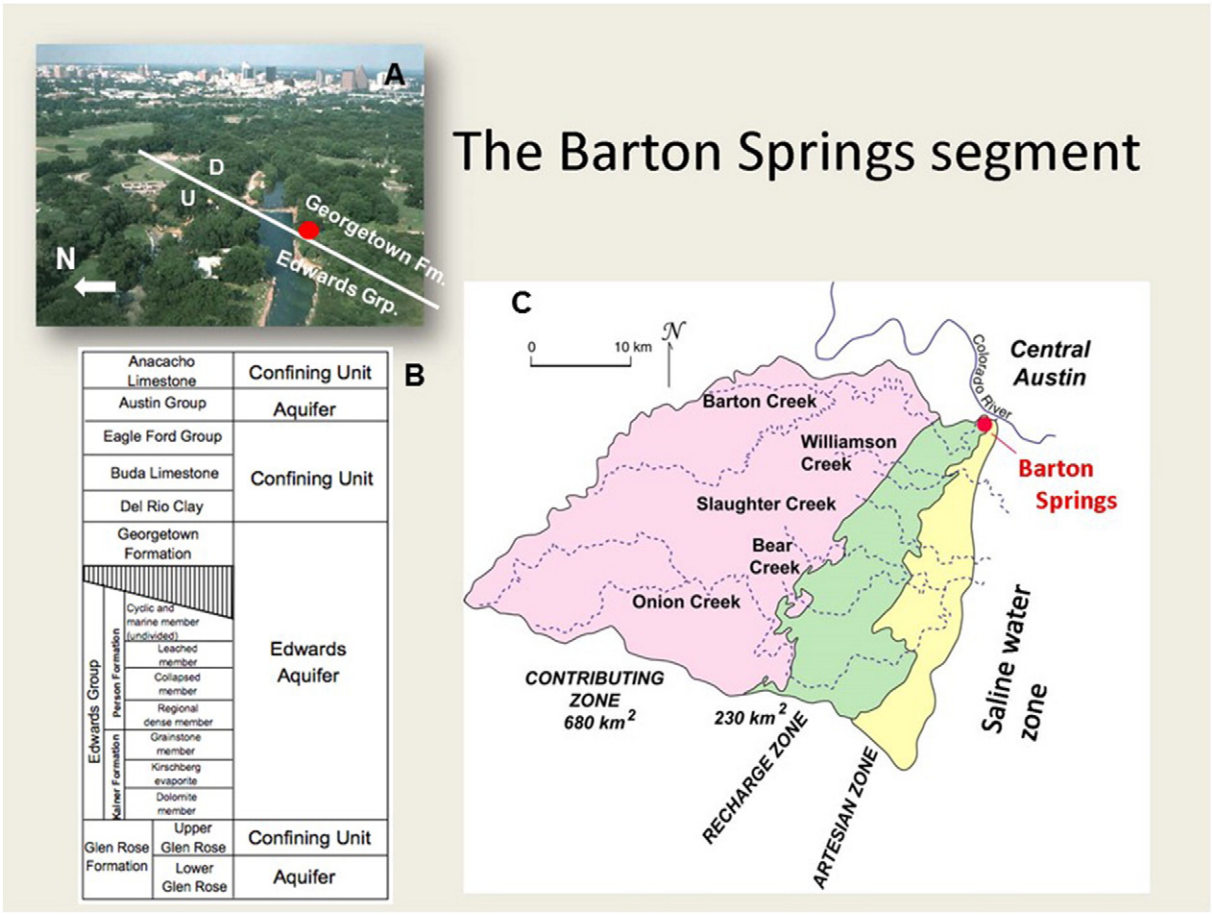

Fig. 2. Map showing the Barton Springs swimming pool and the Barton Springs fault (A), the geological time table for Central Texas (B) and the map (C) showing the boundaries of the contributing, recharge and artesian zones in the Barton Springs Segment (Fig. 2a and c are modified from Mahler and Lynch, 1999; and Fig. 2b is modified from Rose, 1972

array. Resistivity values (ohm-m) are highly affected by several variables, including the presence of water or moisture, and the amount and distribution of pore space in the material, as well as temperature (Rucker and Glaser, 2015).

The Advanced Geosciences, Inc. (AGI) SuperSting R1 resistivity meter was used in this study with a dipole-dipole electrode array. This array is relatively sensitive to horizontal changes in the subsurface (compared to other arrays) and, when the data is inverted, provides a 2-D electrical image of the near- surface geology.

The study area includes the west of the pool across the Barton Springs fault, and south Zilker Park, which is located to the south of the swimming pool. A total of 13 resistivity profiles were surveyed in the study area (Fig. 3). Two of the profiles (L1 and L2) were surveyed across the Barton Springs fault in the western part of the study area. The profile spacing was 50 ft (15 m). Profiles L3A, L3B, L4, L5, L6 and L7 were run approximately from the west to the east, and profiles L8 through L12 were conducted in the north-south directions, respectively. All these profiles were surveyed using the dipole-dipole array with 10 to 15 ft (3 and 4.5 m) electrode spacing, and the profile spacing was generally 50 ft (15 m), except for profiles L3A and L3B. The spacing between these two profiles was 25 ft (7 m).

Resistivity data from E-W and N-S profiles were constructed as 2D resistivity cross-sections and displayed as a 3-dimensional (3D) resistivity block, which represents a "pseudo-3D resistivity" since it is still based on 2D sections, not a full 3D resistivity experiment. AGI's 2D and 3D Earth Imager software were used for processing the resistivity data.

The study of the decaying potential difference as a function of time is now known as the study of induced polarization (IP) in the time domain. In this method the geophysicist investigates for portions of the earth where current flow is maintained for a short time after the applied current is terminated. The induced electrical polarization method is widely used in exploration for ore bodies (Parasnis, 1996, Telford et al., 1990, Bery et al., 2012). Use of IP in geotechnical and engineering applications has been limited, and has been used mainly for groundwater exploration (Dahlin et al., 2002, Xianxin and Kai, 2011).

Induced polarization (IP) surveys were performed along two profiles (L2 and L3A). The data was simultaneously collected during the resistivity surveys. The IP unit used in these surveys is millisecond (ms).

3.2. Self-potential (SP) surveys

Natural electrical currents occur everywhere in the subsurface. Slowly varying direct currents (D.C.) give rise to a surface distribution of natural potentials due to the flow of groundwater within permeable materials, which help locate karstic features, such as caves and sinkholes (Lange and Kilty, 1991, Lange, 1999, Vichabian and Morgan, 2002; and Saribudak, 2011). Differences of potential are most commonly in the millivolts range and can be detected using a pair of non-polarizing copper sulfate electrodes and a sensitive measuring device (i.e. a voltmeter or potentiometer). It should be noted that SP measurements made on the surface are the product of electrical current due to groundwater flow and the subsurface resistivity structure (Atangana et al., 2015).

The SP data were collected along profiles L2, L3A, and L3B. The station spacing was held between 10 and 15 ft (3 and 4.5 m).

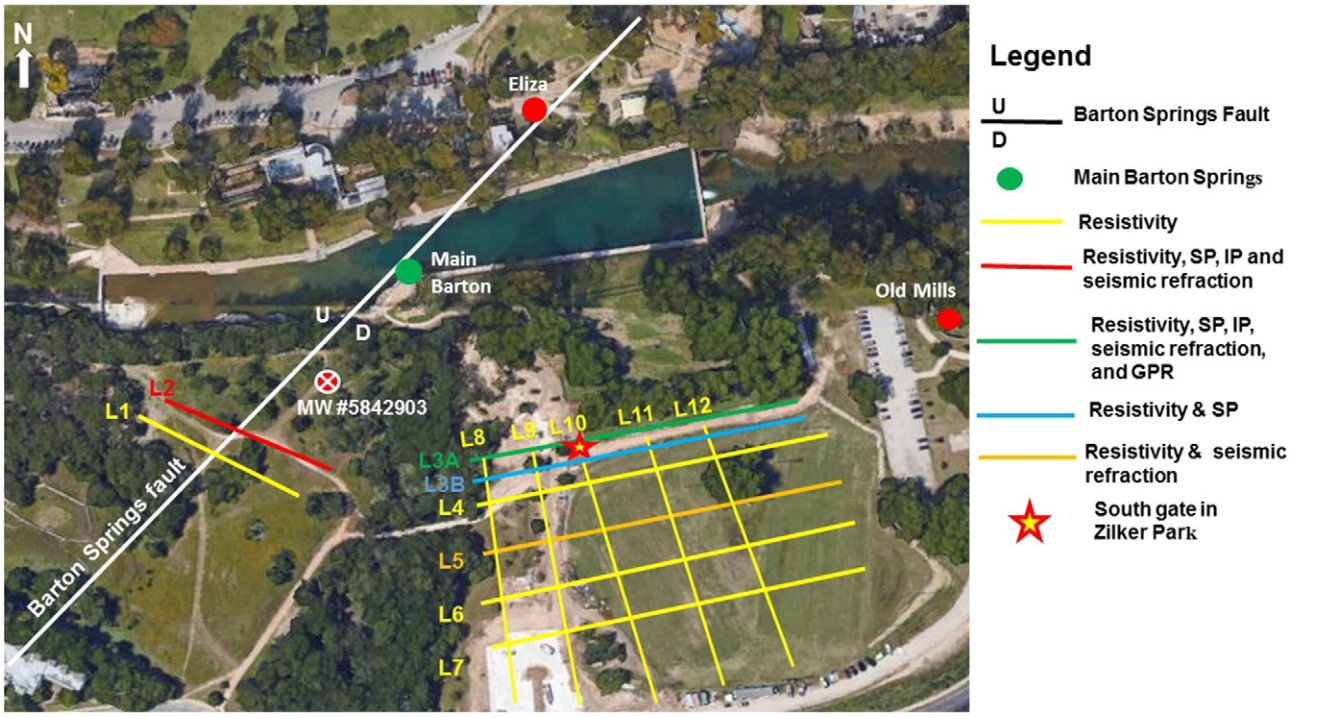

Fig. 3. Map showing the locations of geophysical profiles in the vicinity of the Barton Springs fault and the swimming pool. *Note that the southern part of the Barton Springs pool has been renovated and the current fence line outlining the southern limit of the property was located 50 ft further to the south since the performance of geophysical surveys.*

The results of the SP surveys are presented as a set of profiles, plotting SP values against the distance of measuring electrode. The interpretation is mainly qualitative. The magnitude and sign (+ or −) of SP values are affected by groundwater flow either within a conduit (e.g., void, cave) and/or capillary system (Vichabian and Morgan, 2002). Positive anomalies can represent subsurface water flow, such as a cave or areas of discharge (springs), while negative anomalies may represent areas of infiltration (e.g., cave, sinkhole).

There is no commercially available SP geophysical instrument in the geophysical market. For this reason, a SP system was developed in-house a decade ago and has been successfully utilized since then.

3.3. Seismic refraction

Refraction seismic data were acquired along three profiles L2, L3A, and L5 in the study area. The seismic refraction method identifies lateral and vertical seismic velocity and/or layer thickness changes. It works best in layered geology. Of most importance in the refraction seismic method is the P-wave energy, which is a compressional body wave that has the highest rate of propagation of any seismic waves (Chen and Zelt, 2016). As a P-wave travels through the earth, it moves each particle it traverses in a direction collinear with the direction of propagation as a series of compressions and rarefactions (Parasnis, 1996). The refraction method will only see layers that increase in velocity with depth.

The Geometrics Geode seismic unit was used with 24 geophones at 10-foot (3 m) intervals. Seismic energy is put into the ground with a 14-pound sledgehammer, with impacts made at various distances offset and along the seismic profile for a total of 11 shots. The seismic data were stacked, nominally, five times at each source point to increase the signal-to-noise ratio.

The seismic refraction data was processed using Rayfract software provided by Intelligent Resources, Inc., which utilizes a ray-tracing algorithm for P-waves. The output is a seismic refraction tomography section that displays the seismic velocity model of the subsurface geology, and is produced by using Golden Surfer software.

3.4. Ground penetrating radar (GPR)

Ground penetrating radar (GPR) surveys were also conducted using a 400 megahertz (MHz) antenna with a shallow-survey mode mounted on a survey GSSI cart, with ranges that have a depth penetration of up to 10 ft (3 m). GPR is the general term applied to techniques that employ radio waves in the 1 to 1000 MHz frequency range. GPR is used to map near-surface geology and man-made-features (e.g., Freeland, 2015; Freeland et al., 2016; Lachhab et al., 2015). The GPR system consists of transmitter and receiver antennas, and a colored display unit. Depth penetration of the radio waves is limited by the antenna chosen (the smaller the antenna and higher the frequency, the shallower the depth of exploration) and the conductivity of the soil. The electrical conductivity of the subsurface material determines the depth penetration of the radar signals. In soils and porous rocks electrical conductivity is primarily governed by the water content, clay content and conductivity of the pore water (Rucker and Ferré, 2004). One GPR profile was run along profile 3A from the west to the east direction, and GSSI's Radan software was used for processing.

4. Interpretation of geophysical results

The geophysical data were interpreted in three sections: 1) Across the Barton Springs fault, 2) along the southern and northern banks of the Barton Springs swimming pool, and 3) in south Zilker Park, which is located to the south of the swimming pool.

4.1. Barton Springs fault

Two resistivity profiles were surveyed along L1 and L2. In addition, SP, IP and seismic refraction surveys were also conducted along profile L2.

Fig. 4 shows the resistivity data along profiles L1 and L2 across the Barton Springs fault.

Both resistivity profiles explicitly display the fault location across which the Edwards Aquifer unit is juxtaposed against the Georgetown

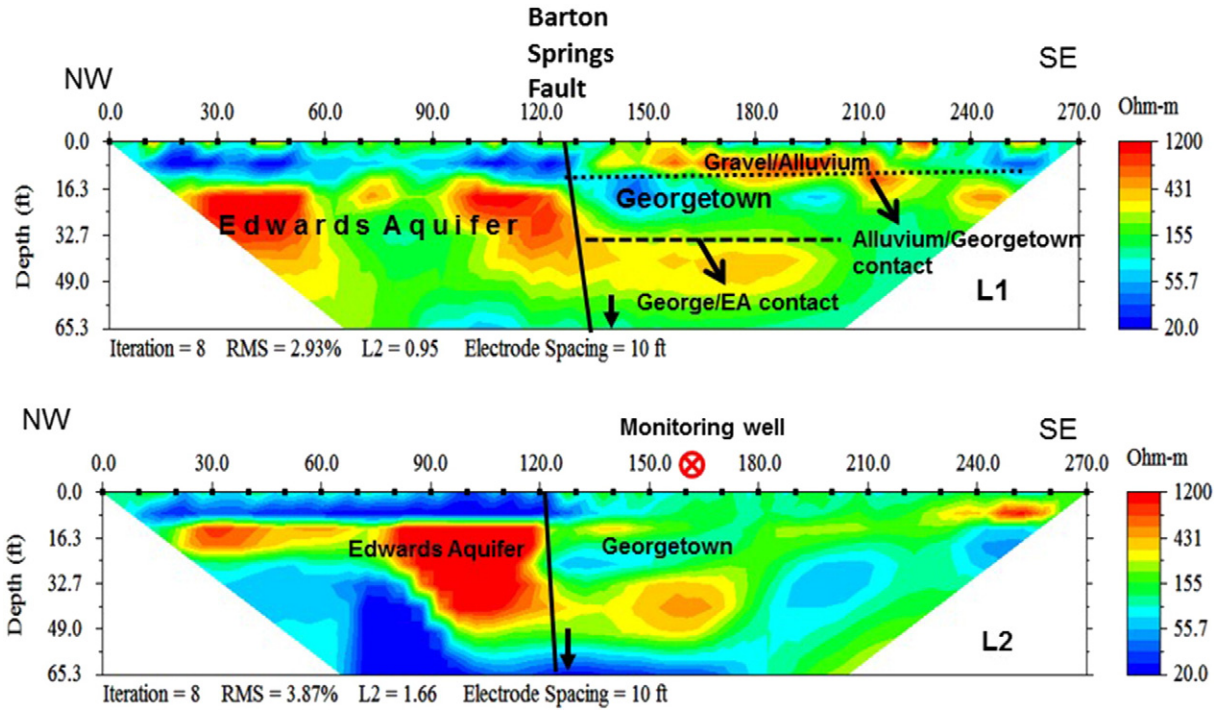

Fig. 4. Resistivity data across the Barton Springs fault along profiles L1 and L2. Note that both resistivity data sets indicate the fault with about 25 ft vertical throw (see text for more information).

Formation with a vertical displacement of 25 ft (7 m). The resistivity data also indicates a veneer of low and high resistivity values between the surface and the depth of 10 ft (3 m), which correspond to the presence of alluvium and gravel materials outcropped in the study area.

A USGS monitoring well (ID #08155500) is located on the downthrown side of the fault and is about 75 ft (23 m) to the east of resistivity profile L2. Interpretation of the monitoring well data suggests a cover of 18 ft (5.5 m) of alluvium over the Georgetown Formation, which is underlain by the Edwards Aquifer units at about 32 ft (10 m) below the surface. It should be noted that the depth to the top of the Georgetown Formation on the downthrown side of the fault along both resistivity sections is about 33 ft (10 m), and correlates well with natural gamma downhole log interpretation from the nearby monitoring well.

The SP data along profile L2 are shown in Fig. 5A. The SP data indicates a regional anomaly across the fault. SP values in millivolt (mV) start with −2 mV at the beginning of the profile, and terminate with a +4 mV value at the end of the profile. SP values appear to increase steadily towards the southeast. The SP data does not indicate any significant anomaly across the fault.

The induced polarization data shows a negative IP anomaly (−34 ms) on the upthrown side of the fault (Fig. 5B). This negative

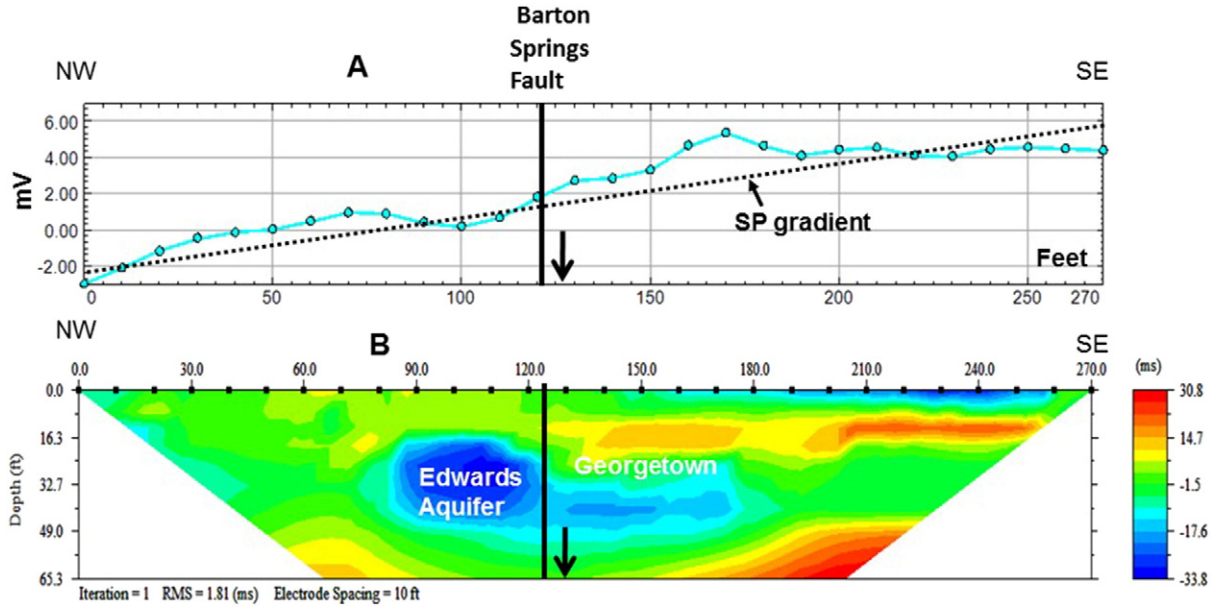

Fig. 5. Self-potential (SP) and induced polarization (IP) data sets across the Barton Springs fault along profile L2. The IP unit is milliseconds (ms) and denotes the chargeability. The SP data (A) does not indicate a significant anomaly across the fault; however, the IP data (B) displays a significant negative anomaly across the fault indicating the geometry of the fault.

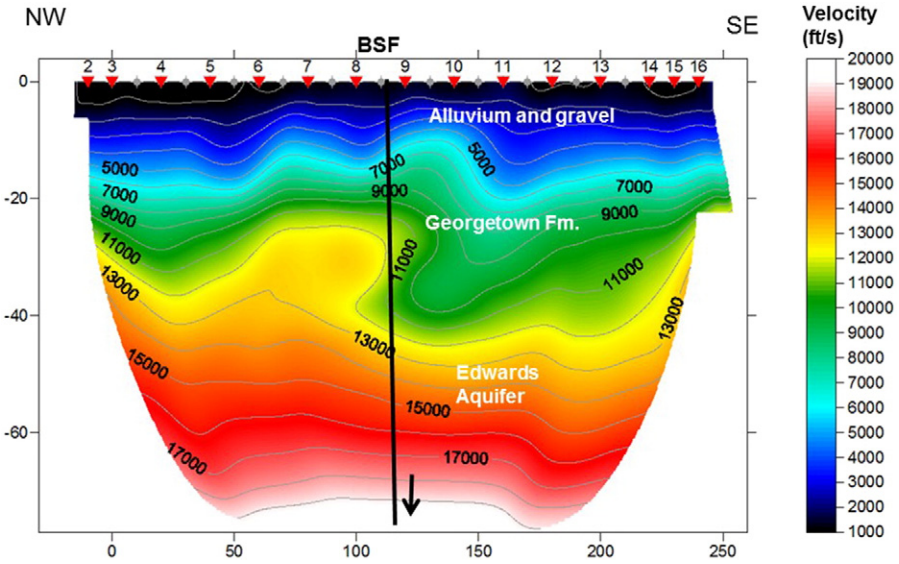

Fig. 6. Seismic refraction data across the Barton Springs fault along profile L2. The seismic data indicates the Georgetown Formation overlies the Edwards Aquifer unit on an uneven paleo-surface on either side of the fault. The fault throw on the seismic section is about 20 ft (6 m).

anomaly loses its magnitude across the fault but it still displays negative values in the downthrown side within the Edwards Aquifer unit (Fig. 5B). The source causing the negative IP anomaly is not known.

The seismic refraction tomography data across the fault is given in Fig. 6, which shows the Georgetown Formation has an average seismic velocity of 10,000 ft/s (3000 m/s), which is overlain with a low velocity layer of 1000 to 5000 ft/s (300 to 1500 m/s). The Edwards Aquifer unit underlies the Georgetown Formation, and has an average velocity of 15,000 ft/s (4500 m/s). The Georgetown Formation overlies the Edwards Aquifer unit on an uneven paleo-surface on either side of the fault. The fault throw on the seismic section is about 20 ft (6 m).

4.2. Self-potential results along the banks of Barton Springs pool and in south Zilker Park

Two SP profiles, crossing the Barton Springs fault, were run on the south and north banks of the swimming pool in order to locate karstic features. Results were published in Saribudak et al., 2013, which indicated a high SP anomaly located on the south bank of the swimming pool. A similar anomaly along the northern bank, across from the pool, was also observed. Both SP profiles also indicate a low SP anomaly in the near vicinity of the Barton Springs fault (see Fig. 14 in Saribudak et al., 2013).

Locations of both high and low SP anomalies are marked on an aerial map of the Barton Springs pool as shown in Fig. 7. It is important to note

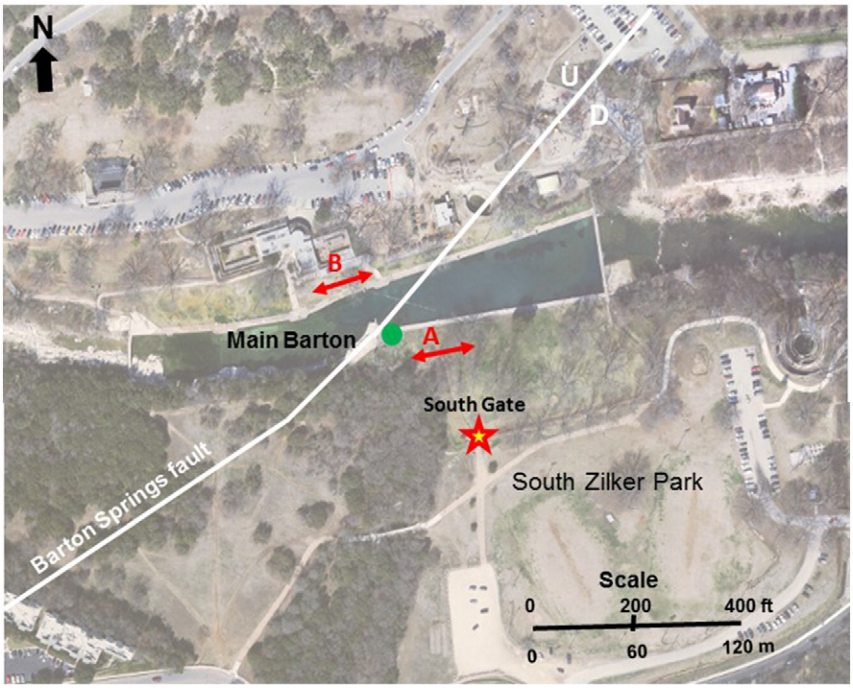

Fig. 7. Approximate transposition of SP anomalies onto an aerial photo of the Barton Springs swimming pool. Note that the high SP anomalies (A and B) face each other across the fault, which could indicate a common source, such as the ground water flowing across the fault via the same conduit.

that the SP anomaly A aligns itself in approximately the same direction as the ground water flows into the swimming pool.

4.3. Geophysical results from south Zilker Park

Because of the presence of the high SP anomaly on the southern bank of the pool, additional geophysical surveys were conducted in south Zilker Park in order to investigate the anomaly's origin. Locations of the geophysical profiles are shown in Fig. 3.

4.3.1. West-east resistivity data

Six 2D resistivity profiles were surveyed in the west-east direction (Fig. 3). The distance between the profiles was kept approximately 50 ft (15 m) except the spacing between profiles L3A and L3B. The distance between those profiles was 25 ft (8 m). The lower and upper resistivity values were also fixed between 1 and 10, 000 Ω·m, except profile L3A.

Fig. 8 shows three resistivity profiles (L3A, L3B, and L4). All profiles indicate a significant low resistivity zone between stations 45 and 135 ft (14 and 41 m). This anomalous location is denoted with the letter A on all three profiles. The low resistivity zone starts at the depth of 25 ft (8 m) and extends as deep as 90 ft (27 m).

Fig. 9 shows the remaining three resistivity profiles (L5, L6, and L7). They, similarly, indicate a low resistivity zone between stations 45 and 135 ft (23 and 41 m). It should be noted that the geometry of the low resistivity zone changes sharply, and its eastern boundary is outlined with a black dashed-line on all resistivity sections.

All six resistivity profiles also have high resistivity anomalies, denoted by a letter B, in the vicinity of the low resistivity anomalies. The sources for both resistivity anomalies are probably due to a combination of significant karst features, such as water-, clay- and air-filled conduits within the Georgetown and Edwards Aquifer units.

The five resistivity data sets were integrated into a 3D resistivity software package and processed. Fig. 10 shows the 3D block diagram, which indicates a well-defined low resistivity zone (anomaly A on 2D cross-sections). The source causing this anomaly is probably a karst conduit as previously discussed. The 3D diagram also indicates a geological contact or a fault immediately located to the east of the south gate of the Barton Springs pool (a heavy-dashed line, see Fig. 10).

4.3.2. GPR and IP data

Ground penetrating radar (GPR) and induced polarization surveys were conducted along profile L3A. The conductivity data was previously published along the same profile in Saribudak et al., 2013, which indicated a metallic pipe anomaly at station 135 ft (41 m) (see Fig. 6 in Saribudak et al., 2013). The conductivity data was further processed by removing the pipe interference in the vicinity of the pipe anomaly. The residual data indicated a significant conductivity contrast on both sides of station 200 ft (61 m). This observation suggests a geological contact or a fault between the high conductivity unit to the east and a low conductivity material to the west.

The GPR data obtained along L3A is shown in Fig. 11, which indicates a fault-like anomaly immediately to the east of the pool gate.

An IP survey was conducted along profile L3A. IP results (Fig. 12) indicate a significant positive anomaly between stations 120 and 180 ft (37 and 55 m). This anomaly is shown in red and its highest magnitude is 181 ms. The top of the IP anomaly is located at about 30 ft (9 m) below surface. Conductivity results from the previous study discussed in Saribudak et al. (2013) indicated a pipe anomaly within the area of the IP anomaly, and it is reasonable to think that the anomaly could be caused by the pipe. But the depth of the pipe should be a few feet below the ground, whereas the IP anomaly is well-seated at about 30 ft, and its width is about 50 ft (15 m). The location of the anomaly correlates well with the low resistivity anomaly of the same profile

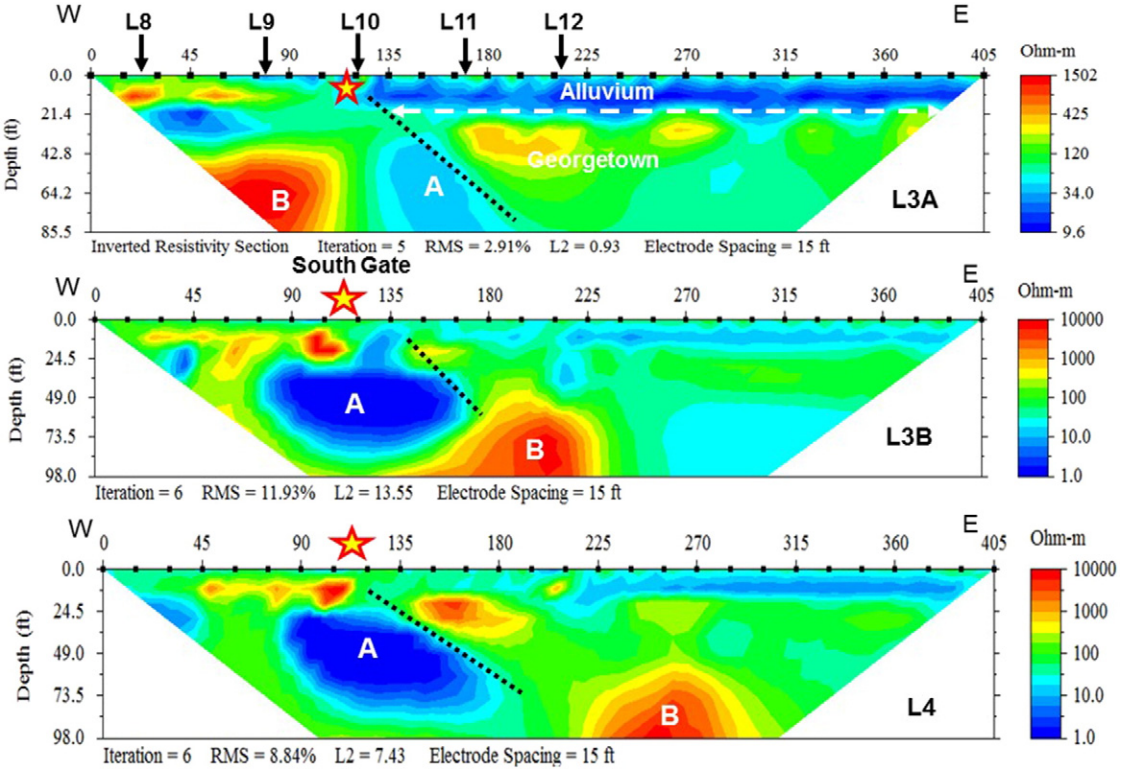

Fig. 8. Three resistivity data sets along profiles L3A, L3B and L4 (see Fig. 3 for location). All three profiles indicate a significant low resistivity anomaly in the vicinity of the south gate entrance. The top soil on the resistivity section appears to be alluvium, which overlies the Georgetown Formation. Locations of north-south resistivity lines (L8 through L12) are also shown. The data for profile L3B was published previously in Saribudak et al., 2013.

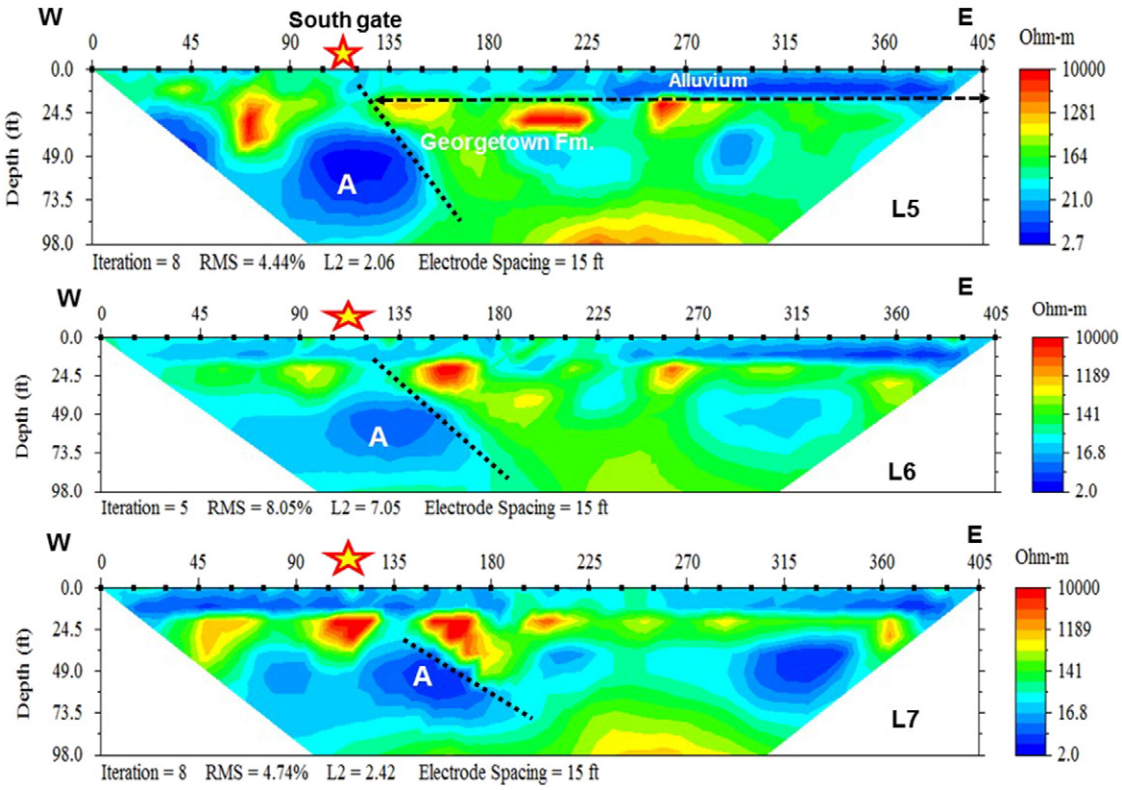

Fig. 9. Three resistivity data sets along profiles L5, L6 and L7. All three profiles indicate a significant low resistivity anomaly in the vicinity of the south gate entrance. See text for explanation. Resistivity profile L7 was published previously in Saribudak et al., 2013.

(see L3A in Fig. 8). Thus the source of the IP anomaly should be geologic in origin.

It should be noted that the GPR data does not indicate any metallic pipe anomaly observed in the conductivity data (see Fig. 11). The E-W resistivity profiles shown in Figs. 8 and 9 did not indicate the presence of any pipe-effect on either the raw or processed data. This observation suggests that the pipe effect on the resistivity and IP data was minimal.

4.3.3. Self-potential data

Self-potential data was collected along profiles L3A and L3B, as displayed in Fig. 13. Both SP data sets indicate a similar, high SP anomaly between stations zero and 200 ft (0 and 61 m). These surveys were done twice in different seasons (winter and summer), using the same base station, and identical data were obtained. These data sets were previously published in Saribudak et al. (2013).

These SP anomalies obtained here are quite similar to those published by Schiavane and Quarto (1984). Their SP anomaly was seen over a fresh water aquifer contact between geological units with differing coupling coefficients. The SP anomalies obtained in this study could also be due to a geological contact (possibly a fault) involving a karst conduit.

4.3.4. Seismic refraction data

The seismic data was collected along two profiles (L3A and L5). These profiles were separated by 100 ft and surveyed to the south of the Barton Springs swimming pool (see Fig. 3 for location).

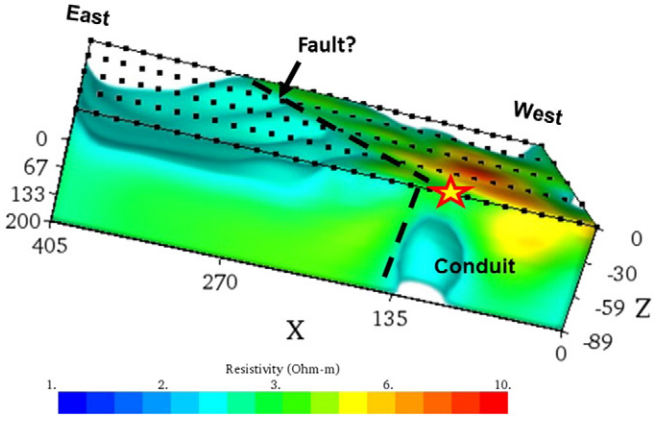

Fig. 10. A pseudo-3-D resistivity block diagram constructed using the 2-D east-west resistivity profiles of Figs. 8 and 9. Note that the 3-D diagram indicates a well-defined low conductivity zone in the direction of the Barton Springs swimming pool near the south gate. The 3-D data also suggest a fault located immediately to the east of the south gate, which is indicated by a star symbol.

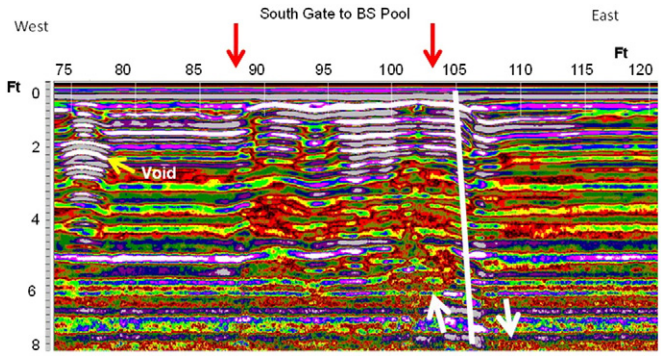

Fig. 11. GPR data along profile L3A. Note the downward bending of the layers at station 105, which is located to the immediate east of the south gate. The source causing this could be either an erosional feature or an existing fault. The red arrows indicate the approximate boundaries of the south gate to the Barton Springs swimming pool.

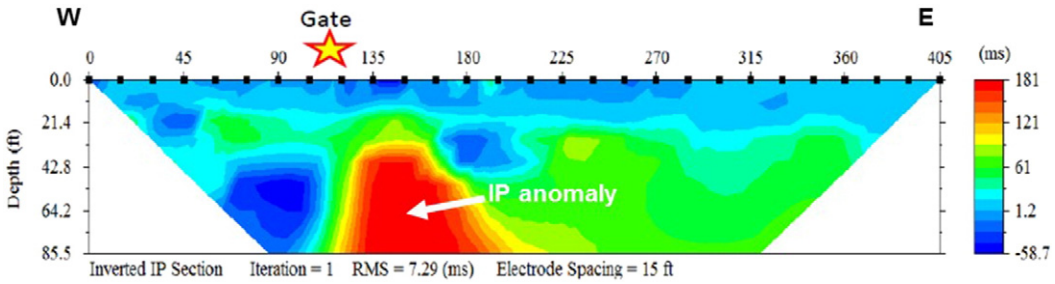

Fig. 12. IP data along profile L3A, which indicates a significant high IP anomaly between stations 115 and 180 ft (35 to 55 m). The top of the IP anomaly is about 30 ft (9 m) and extends all the way down to 85 ft (26 m).

P-wave velocities of the seismic tomography along profiles L3A and L5 show three distinct zones (Fig. 14): 1) Seismic velocities of 2000 and 5000 ft/s (600 and 1500 m/s) are probably due to alluvium deposits (black and blue in color); 2) the low velocity section is underlain by a zone that has a velocity variation between 5000 and 11,000 ft/s (1500 and 3300 m/s) (green in color), which corresponds to the limestone and marly units of the Georgetown Formation; 3) the zone underlying the Georgetown Formation is the Edwards Aquifer limestone unit and shows a velocity range between 11,000 and 18,000 ft/s (3300 and 5500 m/s) (yellow, red and pink in color). The seismic data indicates steeply eastward-dipping layers at about station 100 ft on profile L3A. The source for this anomaly could be due to a fault, with a 25 ft (8 m) throw. The seismic data along profile L5 shows similar velocity layers at similar depths to the seismic data shown on profile L3A. However, seismic velocity layers on profile L5 are horizontal between stations zero and 170 ft (0 to 52 m), after which they appear to terminate sharply with a vertical contact (Fig. 14). This seismic contact could be interpreted as a fault.

It should be noted that the refraction method cannot identify layers or subsurface volumes where velocity decreases, because these volumes or layers will not produce first-arrival head waves. Deeper layers and thicknesses will also be in error. The tomography software used in this work has somewhat mitigated this problem, but a decreased velocity layer in the karstic setting, such as a low resistivity anomaly, may still be a significant "blind spot" for refraction.

4.3.5. North-south resistivity data

Five north-south 2D resistivity profiles were surveyed in the vicinity of the south gate of the Barton Springs swimming pool. Three of the profiles (L8, L9, and L10) were located to the west of the south gate, whereas profiles L11 and L12 were located to the east of the south gate (see Fig. 3 for location). The distance between profiles was approximately 50 ft (15 m). The lower and upper resistivity values are also fixed between 1 and 10, 000 Ω·m, as on the east-west profiles. It should be noted that profiles L9, L10 and L12 were previously published in Saribudak et al., 2013.

Fig. 15 displays the resistivity data along profiles L8, L9 and L10. All three profiles show combinations of significant high resistivity (red in color) and low resistivity (blue in color) anomalies. The common similarity on all three data sets is a bow-like structure between the north and south ends of the profiles (see black dashed lines in Fig. 15). The resistivity anomalies distributed along the profiles appear to be complex and chaotic, and are probably caused by a number of karstic features.

Fig. 16 shows the remaining two resistivity profiles of L11 and L12. The lower and upper resistivity values of these sections were also held between 1 and 10,000 Ω·m. These data sets, in contrast to Fig. 15, do not show significant anomalies. Instead, the resistivity data on L11 and L12 indicate smooth resistivity distribution along the north and south ends of the profiles. The resistivity sections are thus very different from profiles L8 through L10. This observation suggests a structural boundary (fault or contact) to the immediate east of the south gate.

The five 2D resistivity data sets were integrated into the 3D resistivity software and processed. Fig. 17 shows a pseudo-3D block diagram,

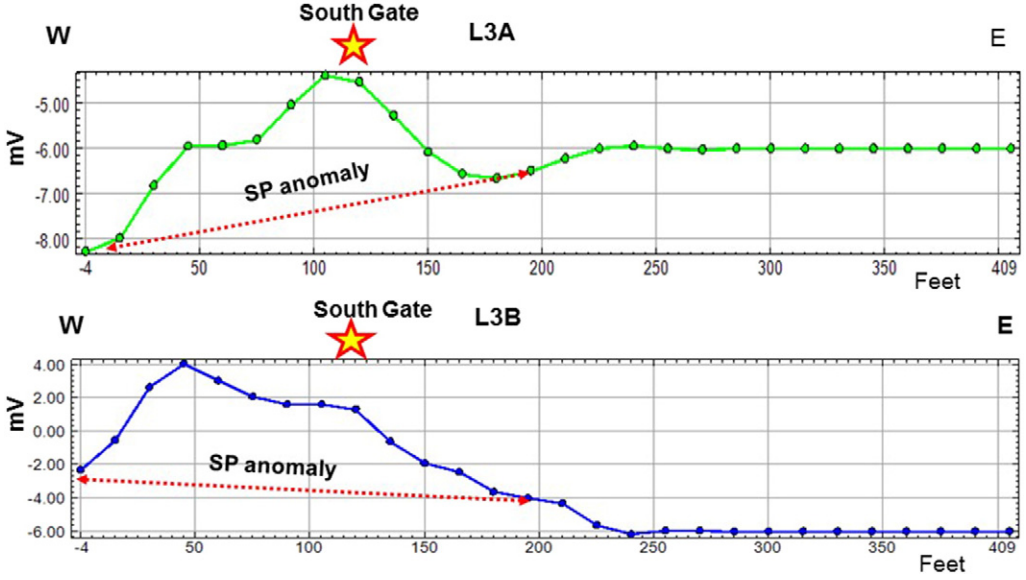

Fig. 13. Two SP data sets along profiles L3A and L3B. Both SP data indicate a peculiar high SP anomaly in the vicinity of the south gate entrance. The high anomaly on both profiles start at about 200 ft (61 m) east of the South Gate and reaches its peak at the south gate location (profile L3A) or immediately to the west of the gate (profile L3B).

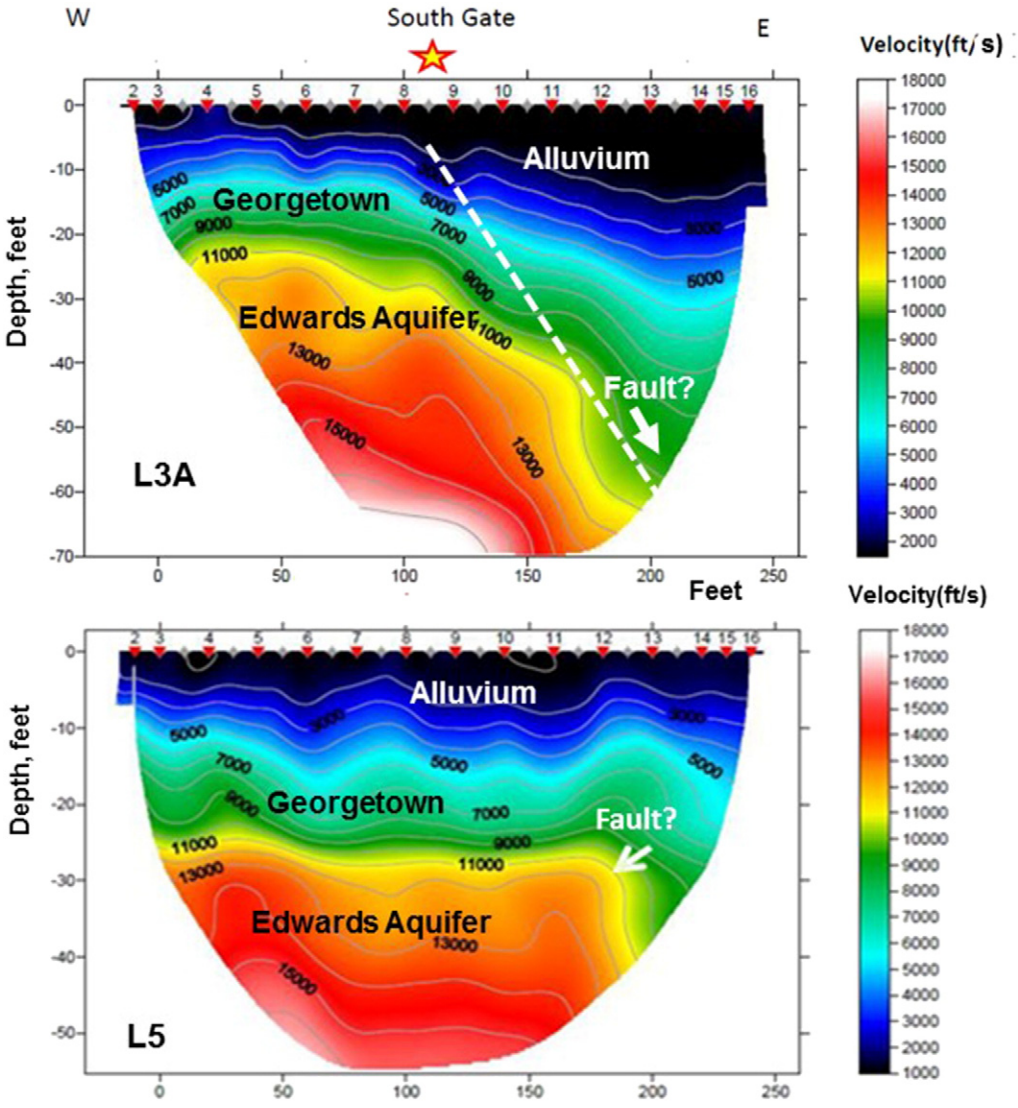

Fig. 14. Seismic refraction data sets along profiles L3A and L5. Profile L3A indicates a fault-like pattern at station 100 ft (30 m). However, profile L5 does not show a similar fault-like anomaly as profile L3A. Instead it displays a sharp contact at about 200 ft (61 m) at the depth of 30 ft (9 m), which could be due to a fault.

which indicates a well-defined low resistivity zone at the northern end of the profiles L8 through L12. The source causing this anomaly could be due to a karst conduit.

It should be noted that an attempt was made to combine the 2D east-west and north-south resistivity profiles in a single 3-D file and run through the EarthImager 3D software. However, this goal was not possible with the commercially available 3D software.

5. Discussion and conclusions

The results of the geophysical surveys across the known location of the Barton Springs fault confirm the presence of the fault. Two resistivity profiles indicate the fault and its 25 ft (8 m) vertical throw. The seismic refraction data defines an irregular paleo-surface between the Georgetown and Edwards Aquifer in the vicinity of the fault. The fault throw displayed by the seismic refraction data is about 20 ft (6 m). The soil thickness overlying the Georgetown Formation is depicted as about 18 ft, which is similar to the monitoring well and the resistivity data. The IP data further confirms the location of the fault. The IP anomaly across the fault, however, is negative in polarity. The lowest magnitude of the IP anomaly corresponds to the upthrown side, where the Edwards Aquifer limestone unit is located. The SP data displays a fault-like anomaly across the Barton Springs fault. There is no significant high SP anomaly across the fault that would indicate karstic features. Thus the absence of the high SP anomaly suggests that the ground water flow across the fault is insignificant.

The offset of the Barton Springs fault, based on the geological observations, is between 20 and 70 ft (6 to 21 m). However, geophysical data indicate the fault throw between 20 and 25 ft (6 and 8 m).

The SP data obtained from the south bank of the Barton Springs pool indicates a significant high and wide SP anomaly (Saribudak et al., 2013). The source for this anomaly can be attributed to the ground water flow within the conduits of Georgetown and/or Edwards Aquifer units.

Six west-east resistivity profiles, which are in the south Zilker Park, indicate significant low and high resistivity anomalies between the west starting points of the resistivity profiles and the south gate located along the southern fence of the pool. The geometry and distribution of these anomalies differ sharply from profile to profile. But they all start at a depth of 25 ft and appear to continue as deep as 98 ft (23 to 30 m). The 3D west-east resistivity diagram indicates a well-defined low resistivity zone (a conduit) and a structural boundary (a fault or geological contact) to the immediate east of the south gate.

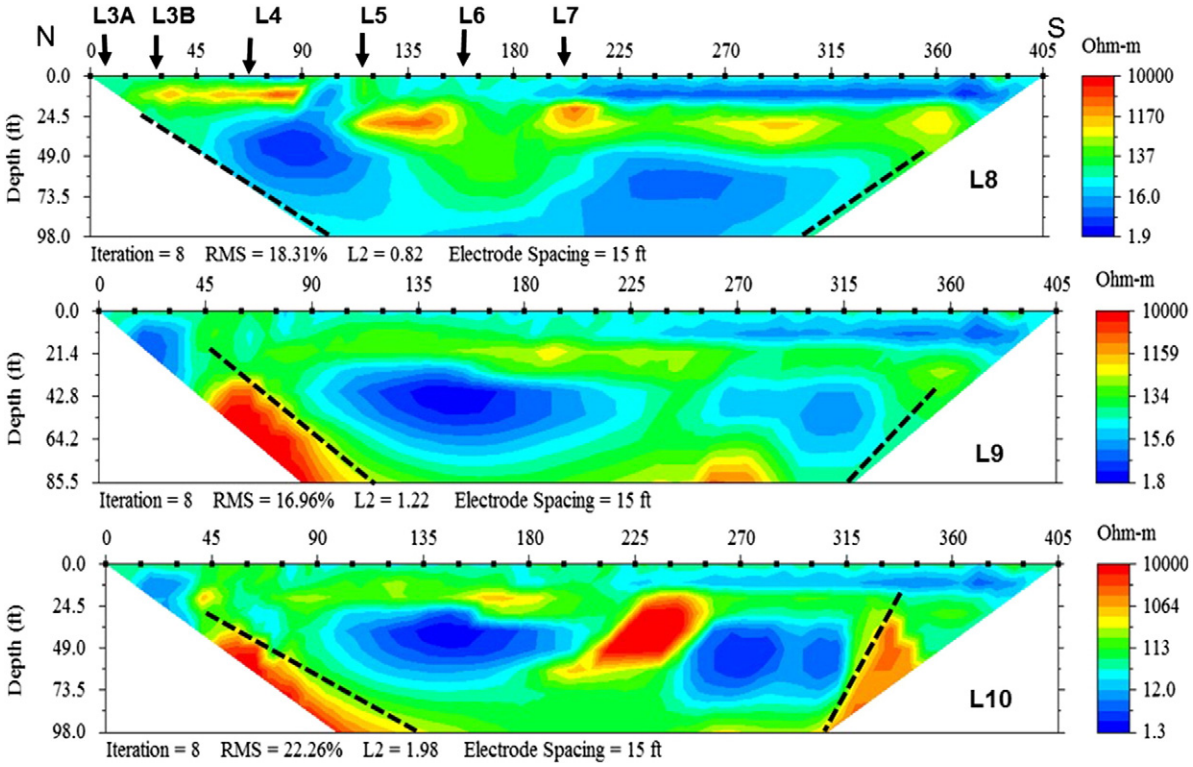

Fig. 15. Resistivity data along profiles L8, L9, and L10 in the north-south direction. All three profiles show combinations of significant low resistivity (blue) and high resistivity (red) anomalies. The common similarity on all three data sets is a bow-like structure between the north and south ends of the profiles. Locations of east-west resistivity lines (L3A, L3B, L4, L5 and L7) are shown. Resistivity profile L10 was published previously in Saribudak et al., 2013.

One IP profile, which was collected along profile 3A, indicates a high IP anomaly, which corresponds to the location of the low resistivity anomaly. The magnitude of this anomaly is significantly high, 181 ms, and its cause is not known.

Two seismic refraction data sets along profiles L3A and L5 contain geological information with regard to the contacts of the geological units in the study area. According to the seismic refraction tomography data, both profiles indicate an average of 10 to 20 ft (3 to 6 m) of alluvium which is underlain by the Georgetown Formation. The Georgetown Formation has a thickness of about 20 ft, and overlies the Edwards Aquifer units. Thus, the thickness of the geological units correlates well with the monitoring data and the resistivity data from the west of the study area over the Barton Springs fault.

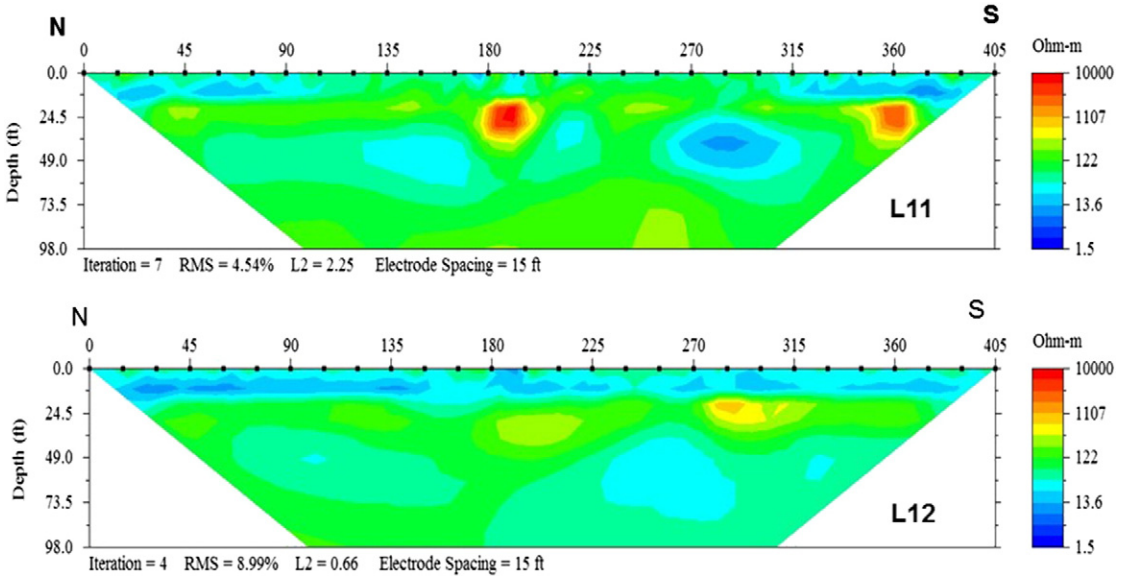

Fig. 16. Two resistivity data sets along profiles L11 and L12 in the north-south direction. These data sets, in contrast to those shown in Fig. 15, do not show significant anomalies. This observation suggests a structural boundary (fault or a geological contact) to the east of the south gate. Resistivity profile L11 was published previously in Saribudak et al., 2013.

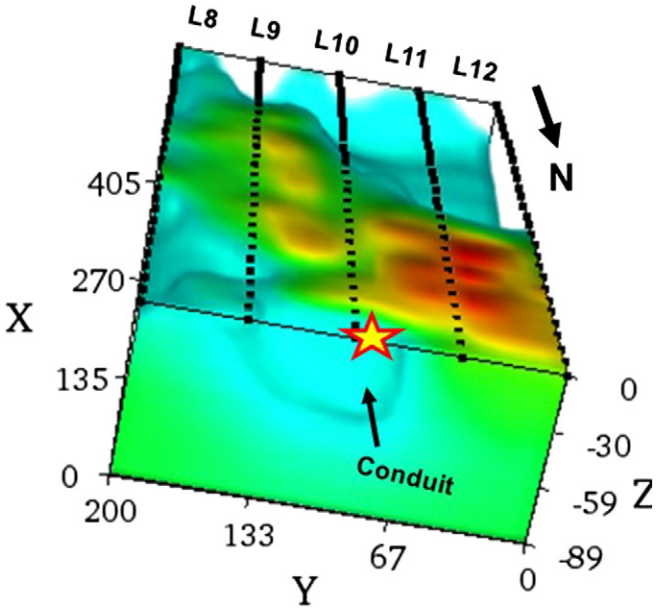

Fig. 17. A pseudo 3-D resistivity block diagram constructed using the 2-D north-south resistivity profiles of Figs. 15 and 16. Note that the 3-D diagram indicates a well-defined low conductivity zone in the direction of the Barton Springs swimming pool in the vicinity of the south gate entrance, which is marked by the star symbol.

Three of the five north-south resistivity profiles in front of the south gate indicate significant low resistivity anomalies along the length of the profiles. There are also high resistivity anomalies associated with the low resistivity anomalies. It should be noted that three resistivity profiles indicate a bow-like geometry. But the remaining two profiles, which are located to the east of the south gate, do not indicate any significant anomaly. The 3D north-south resistivity block indicates a significant low resistivity anomaly (a conduit) in the vicinity of the south gate.

In summary, these geophysical findings indicate significant anomalies to the south of the Barton Springs pool. The majority of these anomalies indicates a fault-like pattern in front of the south gate entrance. The location of geophysical anomalies obtained from surveys performed across the Barton Springs fault and from the area situated to the south of the swimming pool are shown in Fig. 18. Those anomalies reveal significant information on the Barton Springs fault. In addition, geophysical results suggest the presence of a large conduit and a fault in the southern part of the Barton Springs pool. The groundwater flow-path to the Main Springs could follow the locations of those resistivity and SP anomalies along this newly discovered fault instead of the Barton Springs fault, as previously thought. This fault appears to cut the Barton Springs fault obliquely and its western side is upthrown.

In order to support the existence of the new fault with the geological data, elevations of the Georgetown Formation in the downthrown side of the Barton Springs fault were obtained and are shown in Fig. 18. The average elevation of the Georgetown Formation on the northern side of the swimming pool is 423 ft (121 m) above sea level for seven boring locations (David Johns of City of Austin, personal communication, 2015). In the south part of the swimming pool, however, the average elevation value is 453 ft (138 m), and is obtained from five sources (the monitoring well data, an outcrop, two seismic refraction studies, and a resistivity profile) (Fig. 18). A 30 ft (9 m) elevation difference is observed at the downthrown side along the Barton Springs fault between the north and the south areas. If there was no intervening fault, the averaged elevation values of the Georgetown Formation should have similar values on the downward side of the Barton Springs fault across the swimming pool. Instead, the 30 ft (9 m) difference in elevation values of the Georgetown Formation supports the existence of the fault suggested by the geophysical data.

The newly identified fault in south Zilker Park is antithetical to the Barton Springs fault. Antithetic faults have been widely observed in the Balcones Fault Zone, and they typically form after stress release associated with the formation of a synthetic fault and subsequent perpendicular rotation of stress fields (Kulander et al., 1979).

Acknowledgments

We thank Alf Hawkins and Justin Camp for their help during the fieldwork and their enthusiastic support for this project. Our appreciations go to Siegfried Rohdewald of Rayfract Software and Brad Carr for their help in processing the seismic refraction data and the induced

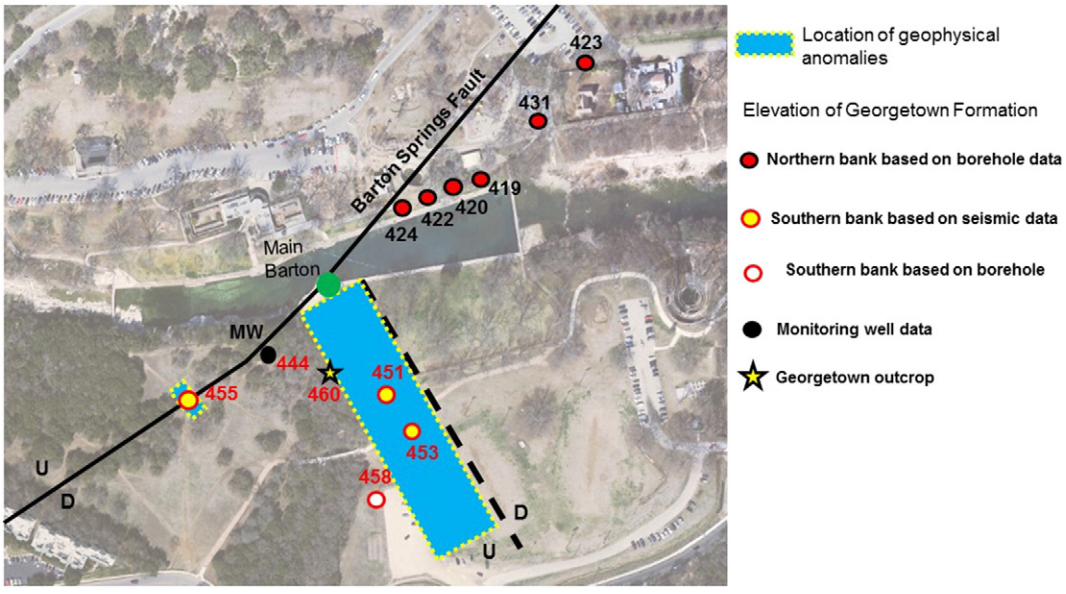

Fig. 18. Map showing the locations of the geophysical anomalies and the elevation values of the Georgetown Formation across the northern and southern parts of the Barton Springs swimming pool. Geophysical anomalies include a fault trending in the NW-SE direction from the south in Zilker Park towards the Barton Springs fault, and a conduit along the fault.

polarization data, respectively. We appreciate Phil Carpenter's review of the manuscript, which helped improve its English and its flow greatly.

We also thank the following colleagues for their help in obtaining the permission to perform the geophysical surveys at the Barton Springs pool and for their eager interest: David Johns, Tom Nelson, Wayne Simmons, Margaret Russell, Sylvia Pope, Nate Benedict, Laurie Dries, and George Veni.

This project was borne out of personal interest and was supported by Environmental Geophysics Associates.

References

Ahmed, S., Carpenter, P.J., 2003. Geophysical response of filled sinkholes, soil pipes and associated bedrock fractures in thinly mantled karst, east-central Illinois. Environ. Geol. 44, 705–716.

Atangana, J.Q.Y., Angue, M.A., Nyeck, B., Ndongue, C., Tchatat, J.T., 2015. Electrical characterization and mineralogical differentiation of a weathering cover in the South Cameroon Humid Intertropical Zone using the self-potential method. J. Environ. Eng. Geophys. 20 (1), 57–70.

Bery, A.A., Saad, R., Mohamad, E.D., Jinmin, M., Azwin, L.N., Tan, N.M.A., Nordiana, M.M., 2012. Electrical resistivity and induced polarization data correlation with conductivity for iron ore exploration. EJGE 17, 3223–3237.

Carpenter, P.J., 1998. Geophysical character of buried sinkholes on the oak ridge reservation, Tennessee. J. Environ. Eng. Geophys. 3, 133–146.

Chen, J., Zelt, C.A., 2016. Application of frequency-dependent Traveltime tomography and full waveform inversion to realistic near-surface seismic refraction data. J. Environ. Eng. Geophys. 21 (1), 1–12.

Connor, C.B., Sandberg, S.K., 2001. Application of Integrated Geophysical Techniques to Characterize the Edwards Aquifer. STGS Bulletin, Texas, pp. 11–25 (March issue).

Dahlin, T., Leroux, V., Nissen, J., 2002. Measuring techniques in induced polarization imaging. J. Appl. Geophys. 50, 279–298.

Dobecki, T., Upchurch, S., 2006. Geophysical applications to detect sinkholes and ground subsidence. Lead. Edge 25 (3), 336–341.

Ferrill, D.A., Morris, A.P., Waiting, D.J., 2005. Structure of the Balcones Fault System and Architecture of the Edwards and Trinity Aquifers, South-Central, Texas. A Field Trip Guide for the South-Central Geological Society of America Meeting.

Freeland, R.S., 2015. Imaging the lateral roots of the orange tree using three-dimensional GPR. J. Environ. Eng. Geophys. 20 (3), 235–244.

Freeland, R.S., Allred, B.J., Martinez, L.R., Gamble, D.L., Jones, B.R., McCoy, E.L., 2016. Performance of hybrid and single-frequency impulse GPR antennas on USGA sporting greens. J. Environ. Eng. Geophys. 21 (2), 57–65.

Garner, L.E., Young, K.P., Rodda, P.U., Dawe, G.L., Rogers, M.A., 1976. Geologic map of the Austin area, Texas, in Garner: an aid to urban planning. Univ. Tex. Austin, Bur. Econ. Geol. scale 1 (65), 500.

Hauwert, N.M., 2009. Groundwater Flow and Recharge within the Barton Springs Segment of the Edwards Aquifer, Southern Travis and Northern Hays Counties, Texas. (A Ph.D. Dissertation). The University of Texas, Austin.

Hauwert, N.M., Johns, D., Hunt, B., Beery, J., Smith, B., Sharp, J.M., 2004. Flow systems of the Edwards Aquifer Barton Springs Segment interpreted from tracing and associated field studies: from Edwards Water Resources. Central Texas, Retrospective and Prospective Symposium Proceedings, San Antonio, Hosted by the South Texas Geological Society and Austin Geological Society (18 pp.).

Hunt, B.B., Smith, B.A., Campbell, S., Beery, J., Hauwert, N., Johns, D., 2005. Dye tracing recharge features under high-flow conditions, Onion Creek, Barton Springs segment of the Edwards aquifer, Hays County, Texas. Austin Geol. Soc. Bull. 5, 70–86.

Johns, D., 2015. Continuous discharge data from Barton Springs and rainfall since 1978. In: Hauwert, N., Johns, D., Hunt, B. (Eds.), Karst and Recharge in the Barton Springs Segment of the Edwards Aquifer: Field Trip to the City of Austin's Water Quality Protection Lands. Austin Geological Society Guidebook 35, pp. 46–49.

Kulander, B.R., Barton, C.C., Dean, S.L., 1979. The Application of Fractography to Core and Outcrop Fracture Investigations: Report Prepared for US DOE (174 pp.).

Lachhab, A., Booterbaugh, A., Beren, M., 2015. Bathymetry and sediment accumulation of Walker Lake, PA using two GPR antennas in a new integrated method. J. Environ. Eng. Geophys. 20 (3), 245–255.

Lange, A.L., 1999. Geophysical studies at Kartchner Caverns State Park, Arizona. J. Cave Karst Stud. 61 (2), 68–72.

Lange, A.L., Kilty, K.T., 1991. Natural Potential Responses of Karst Systems at the Ground Surface. Proceedings of the Third Conference on Geohydrology, Ecology and Monitoring and Management of Ground Water in Karst Terranes: National Groundwater Association pp. 179–196.

Mahler, B.J., Lynch, F.L., 1999. Muddy waters: temporal variation in sediment discharging from a karst spring. J. Hydrol. 214, 165–178.

Musgrove, M., Banner, J.L., 2004. Controls on the spatial and temporal variability of vadose dripwater geochemistry: Edwards Aquifer, central Texas. Geochim. Cosmochim. Acta 68 (5), 1007–1020.

Palmer, N.A., 2007. Cave Geology. Published by Cave Books.

Parasnis, D.S., 1996. Principles of Applied Geophysics. fifth ed. Springer.

Rose, P.R., 1972. Edwards group, surface and subsurface, Central Texas. Report of Investigations 74. Bureau of Economic Geology, Austin, Texas.

Rucker, D.F., Ferré, T.P.A., 2004. Automated water content reconstruction of zero-offset borehole ground penetrating radar data using simulated annealing. J. Hydrol. 309 (1–4), 1–16.

Rucker, D.F., Glaser, D.R., 2015. Standard, random and optimum Array conversions from two-pole resistance data. J. Environ. Eng. Geophys. 20 (3), 207–217.

Saribudak, M., 2011. Urban geophysics: geophysical signature of Mt. Bonnell Fault and its karstic features in Austin, Texas, Houston. Geol. Soc. Bull. (October), 49–54.

Saribudak, M., Hawkins, A., Stoker, K., 2012a. Geophysical signature of Haby Crossing Fault and its implication on the Edwards Recharge Zone, Medina County, Texas. Houston Geophys. Soc. Bull. 2, 9–14.

Saribudak, M., Hunt, S., Smith, B., 2012b. Resistivity imaging and natural potential applications to the Antioch Fault Zone in the Onion Creek/Barton Springs segment of the Edwards Aquifer, Buda, Texas. Gulf Coast Assoc. Geol. Soc. Trans. 62, 411–421.

Saribudak, M., Hauwert, N., Hawkins, A., 2013. Geophysical Signatures of Barton Springs (Parthenia, Zenobia and Eliza) of the Edwards Aquifer. Austin, Texas, Sinkhole Conference 14 Proceedings, Carbonite and EvaporitesSpringer (ISSN 0891-2556).

Schiavane, D., Quarto, R., 1984. Self-potential prospecting in the study of water movements. Geoexploration 22, 47–58.

Small, T.A., Hanson, J.A., Hauwert, N.M., 1996. Geologic framework and hydrogeologic characteristics of the Edwards Aquifer outcrop (Barton Springs Segment), northeastern Hays and southwestern Travis Counties, Texas. U.S. Geological Survey Water Resources Investigations, pp. 96–4306 (15 pp. Prepared in cooperation with the BS/EACD and TWDB).

Telford, W.M., Geldart, L.P., Sheriff, R.E., 1990. Applied Geophysics. second ed. Cambridge University Press.

Thuesen, K., 2013. Restoring land and managing karst to protect water quality and quantity at Barton Springs, Austin, Texas. In: Land, L., Doctor, D., Stephenson, J. (Eds.), Sinkholes and the Engineering and Environmental Impacts of Karst. Proceedings of the Thirteenth Multidisciplinary Conference. National Cave and Karst Research Institute, Carlsbad, New Mexico.

Vichabian, Y., Morgan, F.D., 2002. Self potentials in cave detection. Lead. Edge 23, 866–871.

Xianxin, S., Kai, W., 2011. Induced polarization method applied for groundwater resource exploration, water resource and environmental protection (ISWREP). Int. Symp. 1, 365–368.